



26 **Abstract:**

27 Finite element (FE) analysis can be used to predict bone mechanical environments  
28 that can be used for many important applications, such as the understanding of bone  
29 mechano-regulation mechanisms. However, when defining the FE models, uncertainty  
30 in bone material properties may lead to marked variations in the predicted mechanical  
31 environment. The aim of this study is to investigate the influence of uncertainty in  
32 bone material property on the mechanical environment of bone.

33 A heterogeneous FE model of a mouse tibia was created from micro computed  
34 tomography images. Axial compression loading was applied, and all possible bone  
35 density-modulus relationships were considered through stochastic analysis. The 1<sup>st</sup>  
36 and 3<sup>rd</sup> principal strains ( $\epsilon_1$  and  $\epsilon_3$ ) and the strain energy density (SED) were  
37 quantified in the tibial volume of interest (VOI).

38 The bounds of  $\epsilon_1$ ,  $\epsilon_3$ , and SED were determined by the bounds of the  
39 density-modulus relationship; the bone mechanical environment ( $\epsilon_1$ ,  $\epsilon_3$ , and SED) and  
40 the bone density-modulus relationship exhibit the same trend of change; the relative  
41 percentage differences caused by bone material uncertainty are up to 28%, 28%, and  
42 21% for  $\epsilon_1$ ,  $\epsilon_3$ , and SED, respectively. These data provide guidelines on the adoption  
43 of bone density-modulus relationship in heterogeneous FE models.

44

45 **Keywords:** bone mechanics, material uncertainty, density-modulus relationship,  
46 stochastic analysis

## 47 **1. Introduction**

48 Micro computed tomography ( $\mu$ CT) imaging has become an important tool to  
49 reveal the detailed internal structure of bone, both *ex vivo* and *in vivo* [1, 2].  $\mu$ CT  
50 images can be used to generate micro-finite element ( $\mu$ FE) models, in which the  
51 element size is on the order of micrometers, to investigate the mechanical behavior of  
52 bone, the mechanism of bone mechano-regulation, and the strength of bone after  
53 medical intervention [3-8]. Because the homogeneous  $\mu$ FE models lack realistic  
54 spatial variations in bone properties and exhibit limited accuracy, heterogeneous  $\mu$ FE  
55 models with heterogeneous material properties have been adopted widely in previous  
56 studies [9-11].

57 To generate heterogeneous  $\mu$ FE models of the bone from  $\mu$ CT images, the raw  
58 CT attenuation values must first be related to the bone mineral density (BMD) and  
59 subsequently converted to bone material properties using bone density-modulus  
60 relationship. The relationship between CT attenuation values and BMD values can be  
61 established by first scanning the calibration phantom that contains several rods with  
62 known BMD values provided by the manufacturer, and subsequently fitting a linear  
63 line to the scatter data of the CT attenuation and BMD values of the rods [12]. The  
64 bone density-modulus relationship is typically obtained by first performing a  
65 mechanical testing on the bone samples at the organ-level and subsequently relating  
66 these bone mechanical properties to the various bone densities (apparent density, ash  
67 density, etc.) [13]. Because the mechanical properties obtained from mechanical  
68 testing are apparent values at the organ-level and the microstructures of bone varies  
69 significantly among samples, large variations occur in the bone density-modulus  
70 relationship [9-11, 14]. It is still unclear how these variations affect the predictions of

71 heterogeneous  $\mu$ FE models.

72 The detailed mechanical environment could provide important information for  
73 the full-field validation of bone FE models [15] and for understanding the mechanical  
74 signals driving bone adaptations [16]. For an example, it has been found that bone  
75 sites with high strain energy density (SED) exhibit more activities of bone formation;  
76 on the contrary, low SED leads to bone resorption [16, 17]. However, the uncertainties  
77 in bone density-modulus relationships may affect the mechanical environment  
78 predicted from FE models. To account for these uncertainties, many stochastic  
79 analyses have been performed to assess the effect of variability in material property  
80 on the mechanical environment predicted by FE models [18-21]. However, these  
81 studies focused on either the peak values of the mechanical properties (maximal  
82 principal strains, maximal principal stresses, etc.) or the apparent behavior (fracture  
83 force, hardness, etc.) of the bone samples. The influence of variability in material  
84 properties on the detailed mechanical environment (i.e., the distribution of the 1<sup>st</sup> and  
85 3<sup>rd</sup> principal strains and the strain energy density) across the entire bone spatial space  
86 is still unknown.

87 The aim of this study is to investigate the influence of uncertainty in bone  
88 material property on the detailed mechanical environment of the bone using  
89 heterogeneous  $\mu$ FE models and stochastic analysis.

90

## 91 **2. Materials and methods**

### 92 **2.1 $\mu$ CT image of mouse tibia and image processing**

93 One entire right tibia dissected from a 12-week-old female C57Bl/6 mouse was  
94 imaged using the *ex vivo*  $\mu$ CT imaging system (SkyScan 1172, Bruker, Belgium) with

95 the following setting: a voltage of 49 kV, a tube current of 179  $\mu\text{A}$ , an exposure time  
96 of 1180 ms, and an isotropic image voxel size of 4.3  $\mu\text{m}$ . In preparation for generating  
97 the FE models, the image datasets were processed based on the standard procedure  
98 developed previously [22]. In brief, the tibia was placed back to its anatomic position,  
99 i.e., its long (proximal-distal) axis was aligned along the z-axis approximately, and the  
100 y-z plane passed through the central line of the articular surfaces of the medial and  
101 lateral condyles (**Fig. 1a and b**). This step was to facilitate the application of the  
102 compressive loading along the long axis of the mouse tibia. The image dataset was  
103 subsequently transformed into the new position and resampled using the Lanczos  
104 kernel, which is a low-pass filter and considered to be the “best compromise” among  
105 several simple filters [23].

## 106 **2.2 Generation of heterogeneous finite element models of mouse tibia**

107 The heterogeneous  $\mu\text{FE}$  model of mouse tibia was generated from the  
108 transformed  $\mu\text{CT}$  images (**Fig. 1b and d**). In brief, the grayscale image dataset was  
109 first smoothed with a Gaussian filter (convolution kernel [3 3 3], standard deviation =  
110 0.65) and subsequently binarized into bone and background using a single threshold  
111 value, i.e., 25.5% of maximal grayscale value (approximately 420 mg HA/cm<sup>3</sup>).  
112 However, the tibia cannot be segmented completely using only one threshold value,  
113 because the images includes other bones, such as the femur. Therefore, the tibia and  
114 fibula were further segmented from other bones manually (Amira 5.4.3, FEI  
115 Visualization Sciences Group, France). The tibial–fibula joint and the region of tibial  
116 proximal growth plate were manually filled to allow for load transmission. From the  
117 binarized tibia–fibula images, the  $\mu\text{FE}$  model with the element number of 1,944,774  
118 was created by converting each bone voxel into an eight-node hexahedral element

119 mesh with the element type SOLID185 using an in-house developed Matlab code  
120 (Matlab 2015a, The Mathworks, Inc. USA). The boundary condition was based on the  
121 experimental setup used for the *in vivo* loading of the mouse tibia [7], i.e., all the  
122 nodes on the concave articular surface of the distal tibia were coupled to a distal  
123 reference point (RP), which is constrained in all degrees of freedom; the FE nodes at  
124 the tibial plateau surface were coupled rigidly to a proximal RP, on which a load of  
125 -11 N was applied [7] (**Fig. 1c**). Poisson's ratio for all the materials was set to 0.3.  
126 The uncertainty of the bone's Young's modulus (E) was considered by selecting the  
127 bone density-modulus relationship stochastically, which was an input of the FE  
128 models (**Fig. 1c and d**). The details of this step are described as below.

### 129 **2.3 Stochastic selection of the bone density-modulus relationship**

130 The uncertainty in Young's modulus (E) of the  $\mu$ FE bone models was treated  
131 through a stochastic analysis. First, after matching the anatomic sites, six  
132 density-modulus relationships of the femur and tibia, which were typically adopted in  
133 the literature [13, 14, 24], were reviewed and plotted (**Fig. 2a**). Here, the data on other  
134 anatomic sites, such as the vertebra, were excluded, because these bones have  
135 markedly different structures compared to the tibia and femur.

136 Subsequently, exponential density-modulus relationships were fitted to the  
137 mechanical testing data of the bone samples by adjusting the constants "a" and "b" in  
138 the exponential function (**Equation 1**). Because the  $\mu$ FE model also included hollow  
139 structures of the bone (such as the tibia–fibula joint and the growth plate), which were  
140 generated by the manual filling of these regions in the image processing step, a lower  
141 threshold value of bone ash density of 0.4 g/cm<sup>3</sup> was adopted in the density-modulus  
142 relationship to avoid unrealistically low moduli in the  $\mu$ FE model. The modulus for

143 the elements with bone ash density less than  $0.4 \text{ g/cm}^3$  was set to  $0.0104 \text{ MPa}$  [13].  
 144 Meanwhile, some image voxels may have superficially high grayscale values owing  
 145 to image noise, which lead to unrealistically high bone densities. Therefore, an upper  
 146 threshold value of  $1.2 \text{ g/cm}^3$  was defined in the density-modulus relationship [13]. In  
 147 summary, the exponential density-modulus relationship used in this study was  
 148 formulated as below:

$$149 \quad E = \begin{cases} 0.0104 & \rho_{\text{ash}} < 0.4 \\ a \times \rho_{\text{ash}}^b & 0.4 \leq \rho_{\text{ash}} \leq 1.2 \\ a \times 1.2^b & \rho_{\text{ash}} > 1.2 \end{cases} \quad (1)$$

150 where “a” and “b” are the two constants,  $E$  is Young’s modulus (GPa), and  $\rho_{\text{ash}}$  is  
 151 the bone ash density ( $\text{g/cm}^3$ ). It is noteworthy that based on the conversion between  
 152 bone apparent and ash densities [14], the relationship between bone apparent density  
 153 and bone modulus can also be established and used for the investigations.

154 All possible bone moduli in the heterogeneous  $\mu\text{FE}$  models were considered by  
 155 adjusting the two constants (“a” and “b” in **Equation 1**) within the range covered by  
 156 the various bone density-modulus relationships reviewed (**Figs. 2a and 2b**). This was  
 157 implemented and realized in two steps: first, the intervals of “a” and “b” were  
 158 determined by initially selecting a relatively large interval and subsequently refined  
 159 by optimizing the two constants by the simplex method (**Fig. 2b**) [25]; next, in the  
 160 intervals calculated, “a” and “b” were selected stochastically based on the  
 161 transformation method [26], which has been proven to reduce the computation cost  
 162 effectively. It was found that when “a” changed from 10.22 to 12.07 and “b” changed  
 163 from 1.18 to 2.24, the exponential density-modulus function (**Equation 1**) covered the  
 164 full uncertain interval of the bone density-modulus relationships reviewed (**Fig. 2b**).

165

## 166 **2.4 Calibration of the bone modulus in the finite element models**

167 For each stochastic selection of “a” and “b,” the calcium hydroxyapatite  
168 (HA)-equivalent BMD was calculated at each  $\mu$ CT image voxel using the relationship  
169 established through scanning the calibration phantom. In the present study, the  
170 phantom with rod densities of 0.0 HA mg/cm<sup>3</sup>, 250.0 HA mg/cm<sup>3</sup>, and 750.0 HA  
171 mg/cm<sup>3</sup> was used. The phantom was scanned using the same setting as used for  
172 scanning the tibia. By calculating the image grayscale values at each rod of the  
173 phantom, the relationship of  $\rho_{HA} = 0.0059 \times I_{gray} + 0.242$  ( $\rho_{HA}$  is the  
174 HA-equivalent BMD, of units HA g/cm<sup>3</sup>;  $I_{gray}$  is the image grayscale value) was  
175 established to convert the image grayscale values to HA-equivalent BMD values.  
176 After matching the phantom type and anatomic site, the density-conversion  
177 relationship of  $\rho_{ash} = 0.877 \times \rho_{HA} + 0.079$  was chosen to convert the  
178 HA-equivalent BMD to bone ash density [14]. However, it is noteworthy that  
179 variability exists in this conversion and its influence on the bone mechanical  
180 environment requires further investigations. The modulus for each bone image voxel  
181 was calculated using **Equation (1)** and subsequently mapped to the FE mesh using a  
182 Matlab code developed in-house.

## 183 **2.5 Finite element analysis and post-processing**

184 Based on the stochastic selection algorithm of the transformation method, 11  
185 values were selected for both “a” and “b” in their intervals, thus resulting in 121 bone  
186 density-modulus relationships and 121 FE models. The FE models were solved using  
187 ANSYS (Release 14.0.3, ANSYS, Inc.) on a workstation (Intel Xeon E-5-2670. 2.60  
188 GHz, 256 GB RAM) using the formulation of a linear elastic constitutive model.

189 To investigate the influence of uncertainty in bone material property on the



190 mechanical environment of the mouse tibia, a volume of interest (VOI) was selected  
191 in the FE models. The VOI started from the end of the proximal growth plate and  
192 encompassed 80% of the tibial length (L), which was measured as the distance from  
193 the most proximal pixel of the mouse tibia until the most distal pixel of the mouse  
194 tibia, and is 17.82 mm for the tibia analyzed in the present study (**Fig. 1d**). To  
195 quantify the results in the three-dimensional (3D) bone spatial space, the VOI was  
196 partitioned into 20 compartments of equal length in the z-direction (**Fig. 1e**). Further,  
197 the normalized length of VOI was defined, with the value of zero at the distal end of  
198 the VOI. The 1<sup>st</sup> principal strain ( $\epsilon_1$ ), 3<sup>rd</sup> principal strain ( $\epsilon_3$ ), and SED were selected  
199 as the parameters to describe the mechanical environment of the mouse tibia (**Fig. 1e**),  
200 because  $\epsilon_1$  is likely linked to the bone opening fracture,  $\epsilon_3$  is the compressive strain  
201 reflecting the primary loading scenario in the bone, and SED is highly correlated with  
202 bone adaptations. The averaged values of  $\epsilon_1$ ,  $\epsilon_3$ , and SED in the 20 compartments  
203 were calculated and plotted against the normalized VOI length. The post-processing  
204 of data in this manner is based on the previous findings where the mechanical values  
205 are not reproducible at the image voxel level, but are reliable over a larger VOI [22].  
206 It was found that the bounds of  $\epsilon_1$ ,  $\epsilon_3$ , and SED were determined by the upper and  
207 lower bounds of “a” and “b” and all different selections of “a” and “b” shared the  
208 same upper and lower bounds. Therefore, to determine the bounds of  $\epsilon_1$ ,  $\epsilon_3$ , and SED,  
209 no further refinements on the selection of “a” and “b” were required.

210

### 211 **3. Results**

212 The occurrence frequencies corresponding to the softest and hardest bone  
213 material models are shown in **Fig. 3**. It was found that a lower bone stiffness led to

214 higher  $\varepsilon_1$ ,  $\varepsilon_3$ , and SED. Further, 86% of the nodes in the hardest bone model exhibit  
215 an  $\varepsilon_1$  that is higher than  $250 \mu\varepsilon$  ( $a = 12.07$ ,  $b = 2.24$ ), compared to 89% of the nodes  
216 in the softest bone model ( $a = 10.22$ ,  $b = 2.24$ ). Meanwhile, 83% of the nodes in the  
217 hardest bone model exhibit an  $\varepsilon_3$  lower than  $-250 \mu\varepsilon$  ( $a = 10.07$ ,  $b = 2.24$ ), compared  
218 to 89% of the nodes in the softest bone model ( $a = 10.22$ ,  $b = 1.18$ ). In summary, if  
219 the softest bone model was used instead of the hardest bone model, 3% ( $= 89\% - 86\%$ )  
220 occurrence of  $\varepsilon_1$  were shifted above  $250 \mu\varepsilon$  and 5% ( $= 89\% - 83\%$ ) occurrence of  $\varepsilon_3$   
221 were shifted below  $-250 \mu\varepsilon$ .

222 The material uncertainty-induced bounds of  $\varepsilon_1$ ,  $\varepsilon_3$ , and SED across the tibial VOI  
223 are presented in **Fig. 4**. It was found that when the bone density-modulus relationship  
224 was changed in the FE models, the  $\varepsilon_1$ ,  $\varepsilon_3$ , and SED across the tibial VOI exhibited the  
225 same trend of change (**Fig. 4**). A lower bone stiffness (soft bone) led to an increased  $\varepsilon_1$ ,  
226 an increased SED and a decreased  $\varepsilon_3$ . It is noteworthy that the bounds of  $\varepsilon_1$  and  $\varepsilon_3$   
227 were determined by different bone density-modulus relationships, i.e., the bounds of  
228  $\varepsilon_1$  were determined by  $E = 10.22 \times \rho_{\text{ash}}^{2.24}$  and  $E = 12.07 \times \rho_{\text{ash}}^{1.18}$ , and the  
229 bounds of  $\varepsilon_3$  were determined by  $E = 10.22 \times \rho_{\text{ash}}^{1.18}$  and  $E = 12.07 \times \rho_{\text{ash}}^{2.24}$ .

230 The relative percentage differences (defined as the difference between the  
231 maximal and minimal values divided by the minimal value) of these mechanical  
232 parameters across the tibial VOI are shown in **Fig. 5**. The relative percentage  
233 differences of  $\varepsilon_1$ ,  $\varepsilon_3$ , and SED ranged from 8% to 28%, from 20% to 28%, and from  
234 14% to 21%, respectively (**Fig.5**).

235

## 236 4. Discussion

237 The purpose of this study is to evaluate the effect of uncertainty in bone material

238 property on the mechanical environment of the bone using heterogeneous FE models  
239 and stochastic analysis. This study aims to provide guidelines on the adoption of bone  
240 density-modulus relationship in heterogeneous FE models.

241 Two major findings were revealed from this study. First, we found that if the  
242 softest bone model was used instead of the hardest bone model, 3% occurrence of  $\epsilon_1$   
243 were shifted above 250  $\mu\epsilon$ , and 5% occurrence of  $\epsilon_3$  were shifted below -250  $\mu\epsilon$ . This  
244 affects the study of the bone mechano-regulation mechanism, which was first  
245 proposed by Wolff and Frost [27, 28]. In particular, Frost's mechano-regulation theory  
246 suggests that the local bone mass increases when the strain is above a certain upper  
247 strain threshold, and decreases when the strain is below a certain lower strain  
248 threshold [27]. Furthermore, it has been postulated that the local bone mass is not  
249 responsive of the strain when it is within the interval encompassed by these lower and  
250 upper thresholds, i.e., the "lazy zone" [29]. If -250  $\mu\epsilon$  and 250  $\mu\epsilon$  were set as the  
251 lower and upper bounds of the "lazy zone" [30] respectively, this study implies that  
252 approximately 8% (= 3% + 5%) of the bone voxels will become inactive in the bone  
253 adaptation process if the hardest bone model, instead of the softest model, was used in  
254 the heterogeneous FE models. Therefore, the uncertainty in bone material property  
255 affects the quantification of mechanical stimulation signals of the bone, and is crucial  
256 in the study of the bone mechano-regulation mechanism. Next, we found that owing  
257 to the uncertainty in bone material property, the mechanical environment across the  
258 mouse tibial VOI was changed by up to 28%, 28%, and 21% for  $\epsilon_1$ ,  $\epsilon_3$  and SED,  
259 respectively, thereby indicating the importance of assigning the appropriate bone  
260 properties in studies such as the FE validation study. We also found that the bone  
261 mechanical environment ( $\epsilon_1$ ,  $\epsilon_3$ , and SED) and the bone density-modulus relationship

262 exhibited the same change trend. Therefore, using the bone density-modulus  
263 relationship consistently for defining the bone property could be a feasible strategy in  
264 parametric studies, such as evaluating the effect of medicine intervention on the bone  
265 mechanical behavior [10].

266 It is noteworthy that in the present study, the magnitude of the load applied is 11  
267 N [7] to engender  $1200 \mu\epsilon$  at the medial midshaft of the tibia [31], and thus elicit an  
268 osteogenic response in the mouse tibia [32]. Next, the bone density-modulus  
269 relationships available in the literature are subject-specific and site-specific [33]  
270 because the bone density-modulus relationships are derived from the mechanical  
271 testing of organ-level specimens (e.g., vertebra) in previous studies [34, 35]. Hence, a  
272 universal deterministic bone density-modulus relationship is required that poses a  
273 significant challenge for future research. The universal relationship might be achieved  
274 by the investigations at the bone tissue (microstructural) level. Once the tissue-level  
275 relationship is developed, the accuracy of heterogeneous  $\mu$ FE models will be  
276 increased significantly, because the mapping from bone density to modulus is defined  
277 at the bone-tissue level in the heterogeneous  $\mu$ FE models. Furthermore, in the present  
278 study,  $\epsilon_1$ ,  $\epsilon_3$ , and SED were selected to describe the bone mechanical environment,  
279 because  $\epsilon_1$  is likely to be linked to the mode I (opening) bone fracture,  $\epsilon_3$  is the  
280 compressive strain reflecting the loading scenario performed in this study, and SED is  
281 the resultant bone parameter containing information of both strain and stress that is  
282 highly correlated with bone adaptations [20]. Additionally, a limitation in the present  
283 study is that the FE analysis was only performed under the loading of axial  
284 compression. Other complex loading scenarios, such as the three-point bending, are  
285 not investigated. However, because axial compression was used widely in previous

286 preclinical studies of bone adaptations [7, 10], the results from this study can be  
287 referred easily for a comparison.

288 In summary, uncertainty in the bone material property exhibited a marked effect  
289 on the mechanical environment of the bone, thus implying that the bone  
290 density-modulus relationship should be assigned appropriately in studies such as the  
291 investigation of the bone mechano-regulation mechanism and FE validation. However,  
292 the change trend in the bone mechanical environment is consistent with that of the  
293 bone density-modulus relationship, thus suggesting that assigning bone  
294 density-modulus relationships in the FE models consistently could be feasible for  
295 parametric studies. This study provides guidelines on the adoption of the bone  
296 density-modulus relationship in heterogeneous FE models.

297

### 298 **Conflict of interest**

299 The authors declare that there is no conflict of interest.

300

### 301 **Funding**

302 This study was supported by the National Natural Science Foundation of China (grant  
303 numbers 11702057, 11572077), the Chinese Fundamental Research Funds for the  
304 Central Universities (grant numbers DUT18LK19, DUT17LK11), the Open Fund  
305 from the State Key Laboratory of Structural Analysis for Industrial Equipment (grant  
306 number GZ1611), and the Liaoning Provincial Natural Science Foundation of China  
307 (grant number 2015020141). The raw  $\mu$ CT used in the present study can be obtained  
308 upon the request to the corresponding author.

309

310 **References**

- 311 1. Bouxsein ML, Boyd SK, Christiansen BA, Guldberg RE, Jepsen KJ, Mueller R.  
312 Guidelines for assessment of bone microstructure in rodents using  
313 micro-computed tomography. *J Bone Miner Res* 2010; 25(7): 1468-86.
- 314 2. Lukas C, Ruffoni D, Lambers FM, Schulte FA, Kuhn G, Kollmannsberger P,  
315 Weinkamer R, Mueller R. Mineralization kinetics in murine trabecular bone  
316 quantified by time-lapsed in vivo micro-computed tomography. *Bone* 2013; 56:  
317 55-60.
- 318 3. de Bakker CM, Altman AR, Tseng WJ, Tribble MB, Li C, Chandra A, Qin L, Liu  
319 XS.  $\mu$ CT-based in vivo dynamic bone histomorphometry allows 3D evaluation of  
320 the early responses of bone resorption and formation to PTH and alendronate  
321 combination therapy. *Bone* 2015; 73: 198-207.
- 322 4. Lambers FM, Kuhn G, Weigt C, Koch KM, Schulte FA, Mueller R. Bone  
323 adaptation to cyclic loading in murine caudal vertebrae is maintained with age  
324 and directly correlated to the local micromechanical environment. *J Biomech*  
325 2015; 48: 1179-87.
- 326 5. Lu Y, Boudiffa M, Dall'Ara, Liu Y, Bellantuono I, Viceconti M. Longitudinal  
327 effects of parathyroid hormone treatment on morphological, densitometric and  
328 mechanical properties of mouse tibia. *J Mech Behav Biomed Mater* 2017; 75:  
329 244-51.
- 330 6. Patel TK, Brodt MD, Silva MJ. Experimental and finite element analysis of  
331 strains induced by axial tibial compression in young-adult and old female  
332 C57Bl/6 mice. *J Biomech* 2014; 47: 451-7.

- 333 7. Razi H, Birkhold AI, Zaslansky P, Weinkamer R, Duda GN, Willie BM, Checa S.  
334 Skeletal maturity leads to a reduction in the strain magnitudes induced within the  
335 bone: a murine tibia study. *Acta Biomater* 2015; 13: 301-10.
- 336 8. Willie BM, Birkhold AI, Razi H, Thiele T, Aido M, Kruck B, Schill A, Checa S,  
337 Main RP, Duda GN. Diminished response to in vivo mechanical loading in  
338 trabecular and not cortical bone in adulthood of female C57Bl/6 mice coincides  
339 with a reduction in deformation to load. *Bone* 2013; 55: 335-46.
- 340 9. Easley SK, Jekir MG, Burghardt AJ, Li M, Keaveny TM. Contribution of the  
341 intra-specimen variations in tissue mineralization to PTH- and raloxifene-induced  
342 changes in hardness of rat vertebrae. *Bone* 2009; 46: 1162-9.
- 343 10. Wang N, Rumney RM, Yang L, Robaye B, Boeynaems JM, Skerry TM, Gartland  
344 A. The P2Y<sub>13</sub> receptor regulates extracellular ATP metabolism and the  
345 osteogenic response to mechanical loading. *J Bone Miner Res* 2012; 28(6):  
346 1446-56.
- 347 11. Yang H, Butz KD, Duffy D, Niebur GL, Nauman EA, Main RP. Characterization  
348 of cancellous and cortical bone strain in the in vivo mouse tibial loading model  
349 using microCT-based finite element analysis. *Bone* 2014; 66: 131-9.
- 350 12. Lu Y, Engelke K, Glueer CC, Morlock MM, Huber G. The effect of in situ/in  
351 vitro three-dimensional quantitative computed tomography image voxel size on  
352 the finite element model of human vertebral cancellous bone. *Proc Inst Mech Eng*  
353 *H* 2014; 228(11): 1208-13.
- 354 13. Helgason B, Perilli E, Schileo E, Taddei F, Brynjofsson S, Viceconti M.  
355 Mathematical relationships between bone density and mechanical properties: A  
356 literature review. *Clin Biomech* 2008; 23(2): 135-46.

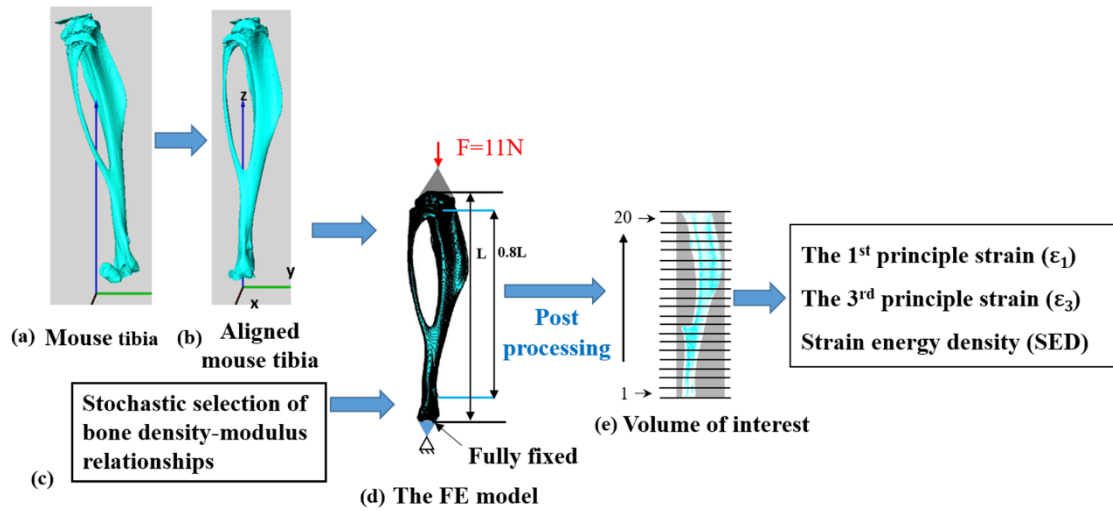
- 357 14. Knowles NK, Reeves JM, Ferreira LM. Quantitative computed tomography  
358 derived bone mineral density in finite element studies: a review of the literature. *J*  
359 *Exp Orthoped* 2016; 3: 36-52.
- 360 15. Costa MC, Tozzi G, Cristofolini L, Danesi V, Viceconti M, Dall'Ara E. Micro  
361 finite element models of the vertebral body: validation of local displacement  
362 predictions. *PLoS One* 2017; 12(7): e0180151
- 363 16. Levchuk A, Zwahlen A, Weigt C, Lambers FM, Badilatti SD, Schulte FA, Kuhn  
364 G, Mueller R. Large scale simulations of trabecular bone adaptation to loading  
365 and treatment. *Clin Biomech.* 2014; 29: 355-62.
- 366 17. Webster D, Wirth A, van Lenthe GH, Mueller R. Experimental and finite element  
367 analysis of the mouse caudal vertebrae loading model: prediction of cortical and  
368 trabecular bone adaptation. *Biomech Model Mechanobiol* 2012; 11: 221-30.
- 369 18. Berthaume MA, Dechow PC, Iriarte-Diaz J, Ross CF, Strait DS, Wang Q, Grosse  
370 IR. Probabilistic finite element analysis of a craniofacial finite element model. *J*  
371 *Theor Biol* 2012; 300: 242-53.
- 372 19. Laz PJ, Stowe JQ, Baldwin MA, Petrella AJ, Rullkoetter PJ. Incorporating  
373 uncertainty in mechanical properties for finite element-based evaluation of bone  
374 mechanics. *J Biomech* 2007; 40: 2831-6.
- 375 20. Taddei F, Martelli S, Reggiani B, Cristofolini L, Viceconti M. Finite element  
376 modeling of bones from CT data: sensitivity to geometry and material  
377 uncertainties. *IEEE Trans Biomed Eng* 2006; 53: 2194-200.
- 378 21. Wille H, Rank E, Yosibash Z. Prediction of the mechanical response of the femur  
379 with uncertain elastic properties. *J Biomech* 2012; 45: 1140-8.



- 380 22. Lu Y, Boudiffa M, Dall'Ara, Bellantuono I, Viceconti M. Development of a  
381 protocol to quantify local bone adaptation over space and time: Quantification of  
382 reproducibility. *J Biomech* 2016; 49: 2095-99.
- 383 23. Turkowski K, Gabriel S. Filters for common resampling tasks. In: Glassner AS  
384 (Ed.), *Graphics Gems 1*. Academic Press 1990; 147-65.
- 385 24. Keller TS. Predicting the compressive mechanical behavior of bone. *J Biomech*  
386 1994; 27: 1159-68.
- 387 25. Cerdà V, Cerdà JL, Idris AM. Optimization using the gradient and simplex  
388 methods. *Talanta* 2016; 148:641–8.
- 389 26. Hanss M, Klimke A. On the reliability of the influence measure in the  
390 transformation method of fuzzy arithmetic. *Fuzzy Set Syst* 2004; 143: 371-90.
- 391 27. Frost HM. Bone's mechanostat: a 2003 update. *Anat Rec A discov Mol Cell Evol*  
392 *Biol* 2003; 275: 1081-101.
- 393 28. Wolff J. Concerning the interrelationship between form and function of the  
394 individual parts of the organism. *Clin Orthop Relat Res* 1988; 228: 2-11.
- 395 29. Beaupre GS, Orr TE, Carter DR. An approach for time-dependent bone modeling  
396 and remodeling application: a preliminary remodeling simulation. *J Orthop Res*  
397 1990; 8: 662-70.
- 398 30. Geraldles DM, Phillips AT. A comparative study of orthotropic and isotropic bone  
399 adaptation in the femur. *Int J Numer Method Biomed Eng* 2014; 30: 873-89.
- 400 31. Fritton JC, Myers ER, Wright TM, van der Meulen MC. Loading induced  
401 site-specific increases in mineral content assessed by microcomputed tomography  
402 of the mouse tibia. *Bone* 2005; 36: 1030-8.

- 403 32. Sugiyama T, Saxon LK, Zaman G, Moustafa A, Sunter A, Price JS, Lanyon LE.  
404 Mechanical loading enhances the anabolic effects of intermittent parathyroid  
405 hormone (1-34) on trabecular and cortical bone in mice. *Bone* 2008; 43: 238-48.
- 406 33. Eberle S, Göttliger M, Augat P. An investigation to determine if a single  
407 validated density-elasticity relationship can be used for subject specific finite  
408 element analyses of human long bones. *Med Eng Phys* 2013; 35: 875-83.
- 409 34. Morgan EF, Bayraktar HH, Keaveny TM. Trabecular bone modulus-density  
410 relationships depend on anatomic site. *J Biomech* 2003; 36: 897-904.
- 411 35. Schileo E, Dall'Ara E, Taddei F, Malandrino A, Schotkamp T, Baleani M,  
412 Viceconti M. An accurate estimation of bone density improves the accuracy of  
413 subject-specific finite element models. *J Biomech* 2008; 41: 2486-91.  
414

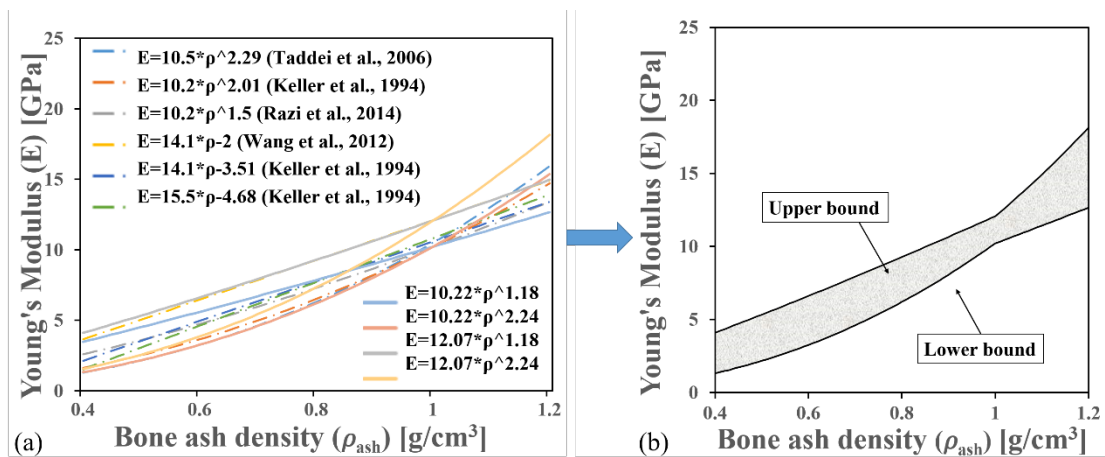
415



416

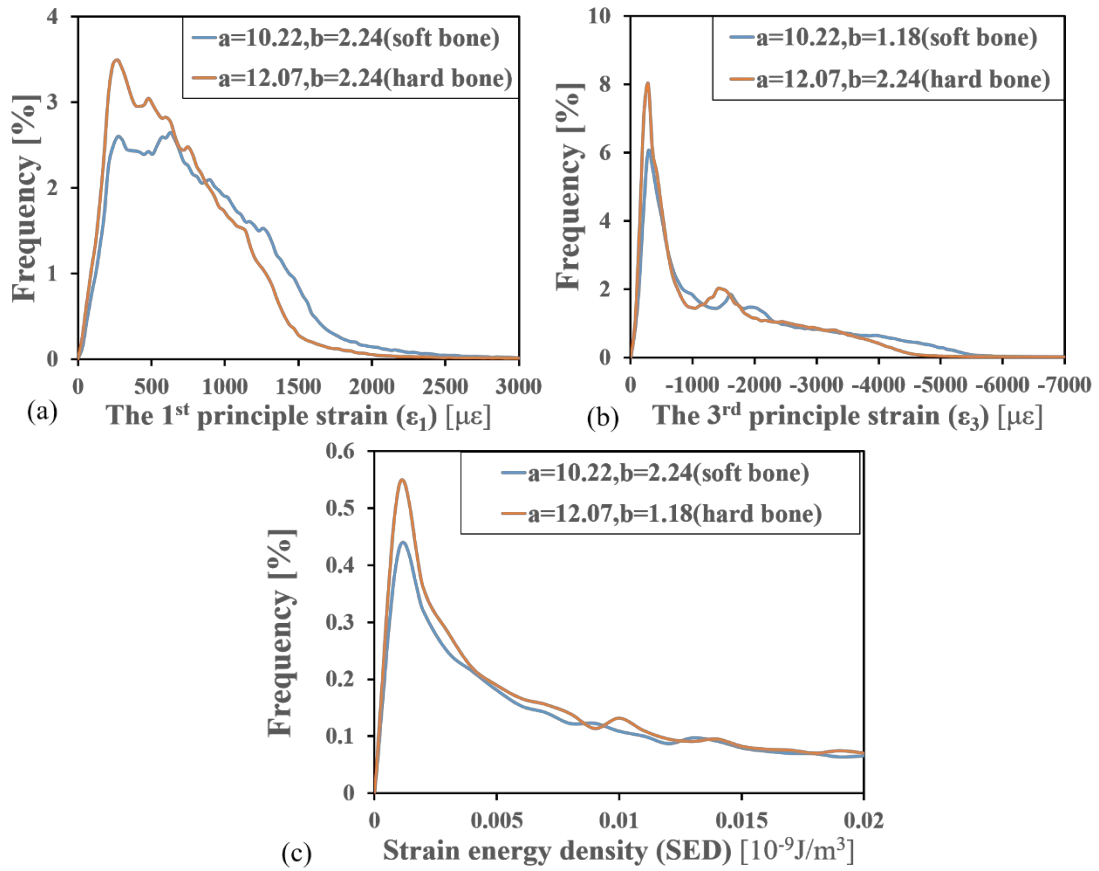
417 **Fig. 1.** Schematic description of the image processing procedure. (a) The mouse tibia;  
 418 (b) the tibia was aligned along the global coordinate system; (c) and (d) the  $\mu$ FE tibial  
 419 model and boundary conditions; (e) the volume of interest (VOI) was partitioned into  
 420 20 compartments and the mechanical environment of the bone was quantified in the  
 421 20 compartments.

422



423

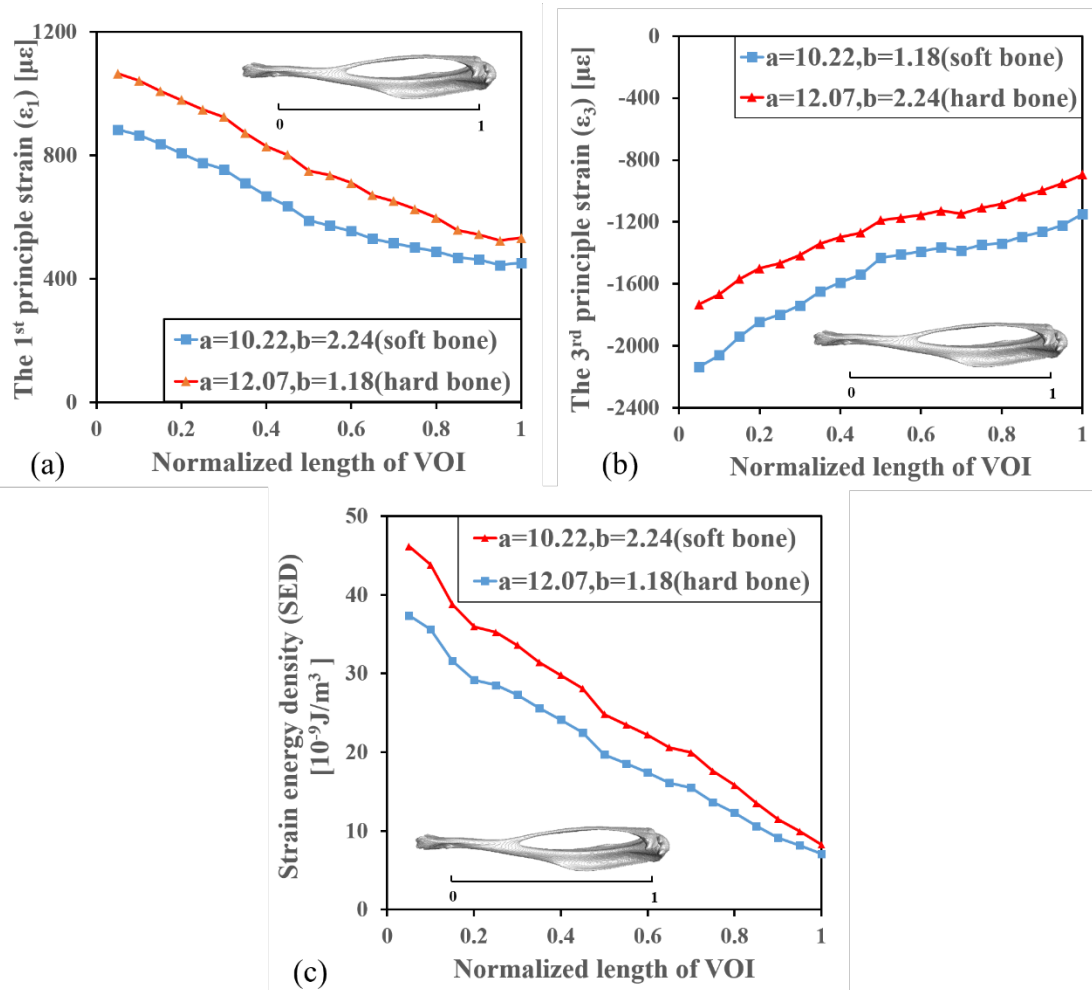
424 **Fig. 2.** Determination of the uncertain interval for the bone density-modulus  
 425 relationships. (a) Fitting exponential functions to the density-modulus relationships  
 426 available in the literature; (b) the determined bone density-modulus interval.



428

429 **Fig. 3.** The influence of material uncertainty on the occurrence frequency of the 1<sup>st</sup>  
 430 principal strain, the 3<sup>rd</sup> principal strain, and the strain energy density. The plotted  
 431 curves of occurrence frequency are the ones with the hardest and softest bone  
 432 density-modulus relationships.

433



434

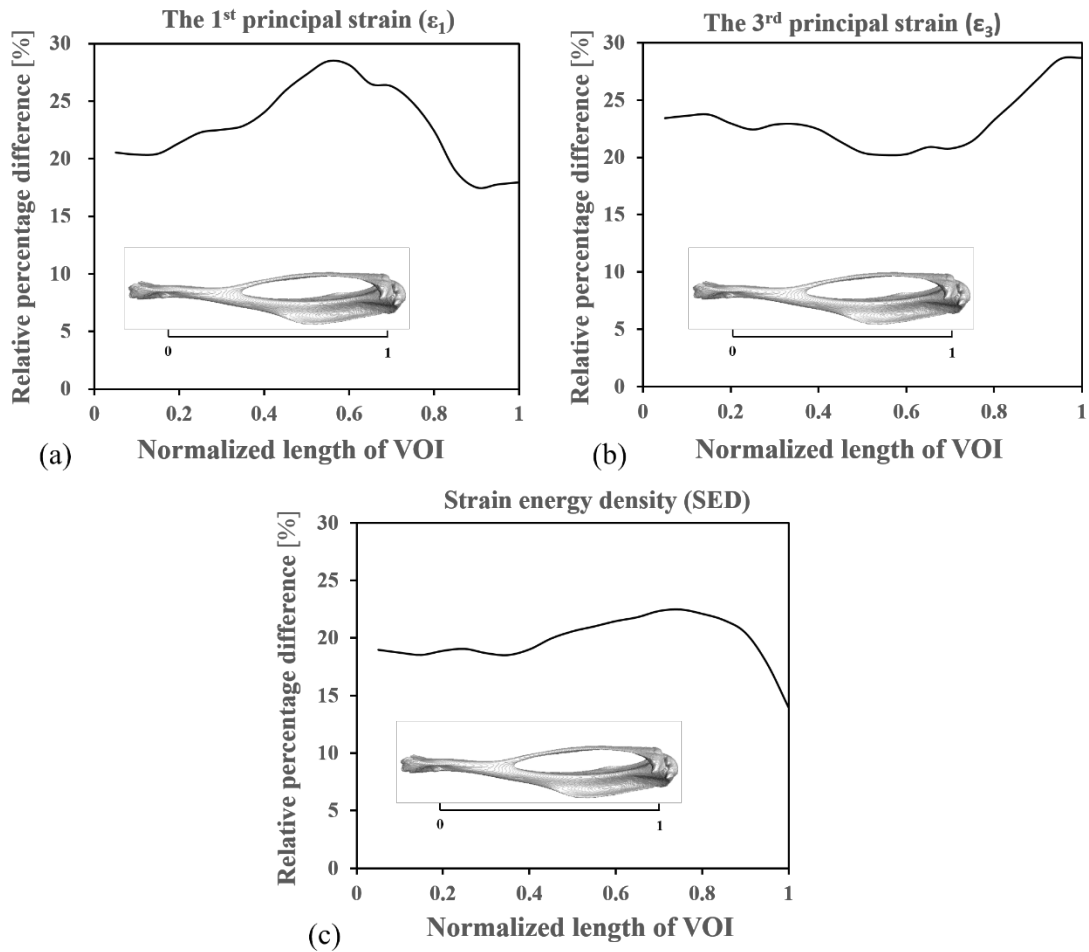
435 **Fig. 4.** The material uncertainty-induced bounds of the 1<sup>st</sup> principal strain, the 3<sup>rd</sup>

436 principal strain, and the strain energy density across the tibial volume of interest

437 (VOI), with the corresponding density-modulus relationships. The dotted data are the

438 mean values in the 20 compartments across the tibial VOI.

439



440

441 **Fig. 5.** The relative percentage differences of tibial mechanical parameters across the  
 442 tibial volume of interest (VOI). Data are presented as the differences between the  
 443 maximal and minimal values divided by the minimal values in the 20 compartments  
 444 across the tibial VOI.